Programmed Assembly of $IrAu_{12}$ Nanoclusters into Dimers and Trimers: Electron Microscopy Observation and Spectroscopic Characterization

Yuto Fukumoto,[1] Shinjiro Takano,[1] Yosuke Asami,[1] Haru Hirai,[1] Koji Harano,[2,3*] and Tatsuya Tsukuda[1*]

[1] Department of Chemistry, Graduate School of Science, The University of Tokyo, 7-3-1 Hongo, Bunkyo-ku, Tokyo 113-0033, Japan.

[2] Center for Basic Research on Materials, National Institute for Materials Science, 1-1 Namiki, Tsukuba, Ibaraki 305-0044, Japan.

[3] Research Center for Autonomous Systems Materialogy, Institute of Integrated Research, Institute of Science Tokyo, 4259 Nagatsuda-cho, Midori-ku, Yokohama, Kanagawa 226–8501, Japan

Supporting Information Placeholder

ABSTRACT: Ligand-protected gold nanoclusters have attracted attention as building blocks for functional materials. In this study, we have demonstrated the programmed assembly of the icosahedral $Ir@Au_{12}$ nanoclusters into a dimer, a linear trimer, linear oligomers, or a triangular trimer via the reaction between the $IrAu_{12}$ with predefined binding sites and bi- or tri-dentate isocyanide linkers. The formation of the intended structures was confirmed by high-angle annular dark-field scanning transmission electron microscopy using a newly developed sampling protocol. Statistical analysis of the inter-particle distances provided quantitative structure models consistent with the theoretically predicted structures. The linear oligomers exhibited a new absorption peak at ~480 nm. Theoretical calculations indicated that the electron transfers from the $IrAu_{12}$ moiety to the linker ligand or another $IrAu_{12}$ moiety involve the absorption. This study demonstrates that programmed assemblies of Au nanoclusters will provide an opportunity to elucidate how novel collective properties arise through assembly.

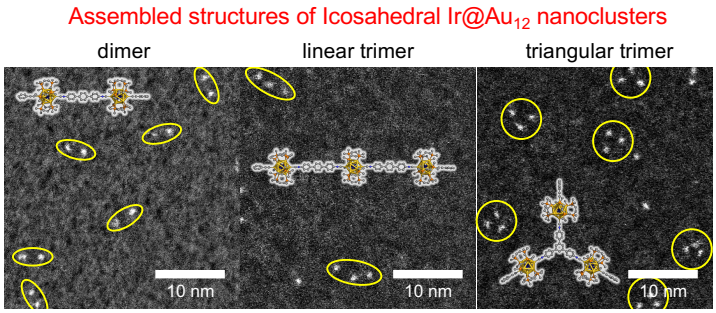

Keywords: Gold Nanoclusters, Programmed Assembly, Transmission Electron Microscopy, Photoinduced Intercluster Electron Transfer

Atomically-precise gold nanoclusters (AuNCs) modified with organic ligands have attracted increasing attention as promising building blocks for functional materials due to their size-specific and tunable properties.[1–4] Recently, many efforts have been made to assemble the AuNCs into controlled structures to tune their collective properties.[5–13] One approach is to self-assemble atomically-precise AuNCs into an ordered, three-dimensional lattice via supramolecular and electrostatic interactions.[14–17] Park's group successfully synthesized the Au_{25}-based coordination frameworks and found an enhancement of the photoluminescence quantum yield depending on the packing mode.[17] These studies have raised the fundamental question of how the collective properties of the assemblies evolve as a function of the number of constituent AuNCs. Assembled structures of countable numbers of AuNCs have been synthesized by ligand exchange with multidentate linker ligands or by coupling reactions on the ligand layer.[18–24] However, it is challenging to assemble atomically-precise AuNCs in a programmed manner with respect to the number, spacing, and symmetry of the constituents.

A promising method for programmed assembly of the NCs is the use of chemically-modified NCs with well-defined exposed sites. The number of exposed sites on the NCs defines the number of directly connected NCs, while the spacing and symmetry of the NCs can be designed by the structure of the linker ligand. The building units in this study are $[IrAu_{12}(dppe)_5(PA)_1]^{2+}$ (**1***) and $[IrAu_{12}(dppe)_5]^{3+}$ (***1***), which were produced by desorption of the PA ligand(s) from $[IrAu_{12}(dppe)_5(PA)_2]^{+}$ (**1**; dppe = $(Ph)_2PC_2H_4P(Ph)_2$, PA = PhC≡C) (Scheme 1).[25] Note that ***1*** has two exposed sites (*) on the opposite sides of the icosahedral $Ir@Au_{12}$ core. We did not use the corresponding pure AuNCs, $[Au_{13}(dppe)_5(PA)_1]^{4+}$ and $[Au_{13}(dppe)_5]^{5+}$, because they could not be synthesized as efficiently as the $IrAu_{12}$ NCs.[25] We then attempted to synthesize the dimer and linear trimer of the $IrAu_{12}$ NCs using 4,4″-*p*-terphenyldiisocyanide (L1) as a linker, according to Schemes 1a and 1b, respectively. The successful formation of the dimer and trimer was confirmed by electrospray ionization mass spectrometry (ESI-MS) and ^{1}H NMR spectroscopy. However, transmission electron microscopy (TEM) observation[18,20–23,26–32] of the dimer and trimer assemblies with the desired structures

failed because the densely aggregated TEM images prevented us from assigning which NCs belonged to the same assembly. Therefore, it remains a technical challenge to visualize the assembled structures of NCs to confirm that the desired structure is being generated quantitatively.

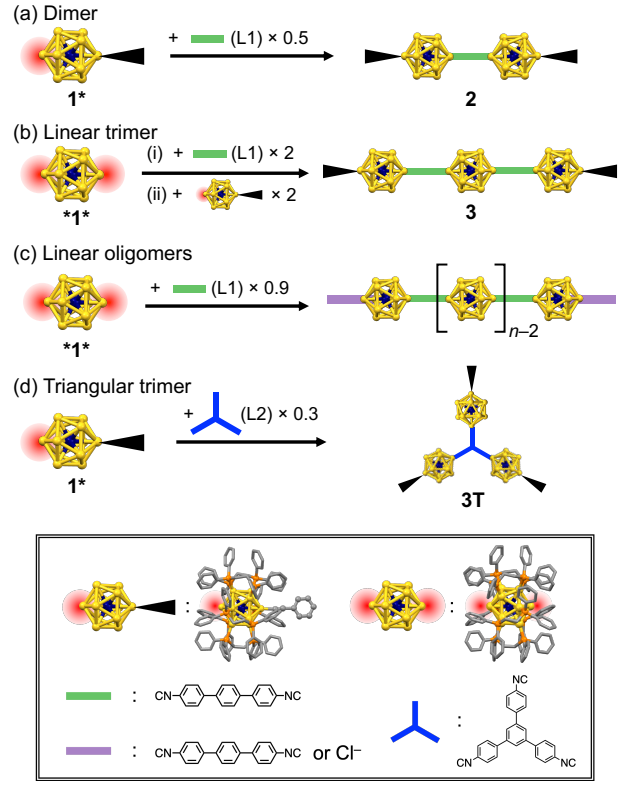

Scheme 1. Synthetic schemes of the ligand-bridged $IrAu_{12}$ assemblies. Color code for the atoms: yellow, Au; dark blue, Ir; light blue, Pd; orange, P; gray, C. Abbreviations used are summarized in Table S1.

In this work, we synthesized the dimer, linear trimer, and linear oligomers of $IrAu_{12}$ NCs using diisocyanide L1 (Schemes 1a–1c) and the triangular trimer using 1,3,5-tris(isocyanophenyl)benzene (L2) (Scheme 1d). We then attempted to visualize the assembled structures by high-angle annular dark-field scanning transmission electron microscopy (HAADF-STEM) by developing a new preparation method of

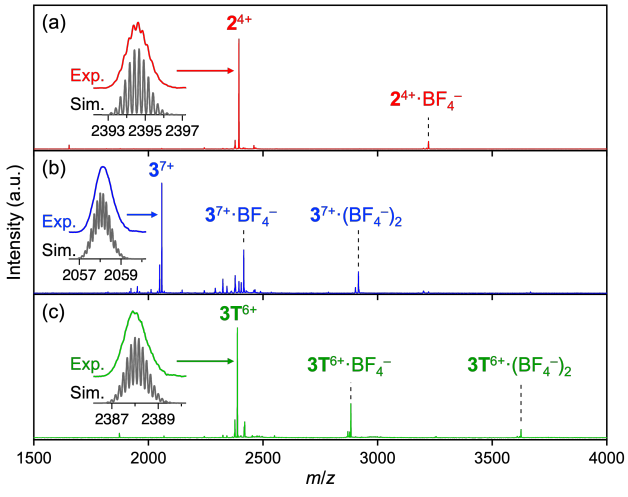

Figure 1. ESI mass spectra of (a) dimer **2**, (b) linear trimer **3**, and (c) triangular trimer **3T**. The *m*/*z* values of the main peaks are summarized in Table S2.

TEM samples: the assembled structures could be sparsely dispersed on the carbon grid by drying the sample solution containing polystyrene (PS) on it. In addition, statistical analysis of the nearest neighbor distance (NND) of $IrAu_{12}$ units confirmed the formation of the expected assembled structures. UV-Vis spectroscopy and density functional theory (DFT) calculations revealed that the assembled dimer and trimer exhibit photo-induced electron transfer from $IrAu_{12}$ to L1 and to $IrAu_{12}$, respectively, in addition to the local excitation within the $IrAu_{12}$ unit.

The assemblies of $IrAu_{12}$ were synthesized from **1*** and ***1*** by the methods summarized in Scheme 1. The dimer **2** and the linear trimer **3** with the structures of **1***–L1–**1*** and **1***–L1–***1***–L1–**1***, respectively, were prepared by the reported method.[25] A new triangular trimer **3T** with the structure of (**1***)$_3$-L2 was synthesized by mixing **1*** with 0.3 equivalents of L2. In the ESI mass spectra, the peaks of the expected dimers or trimers and the adducts with the counteranion BF_4^- were observed as main products (Figure 1). In the ^{1}H NMR spectra, the signals of dppe, PA, and L1 or L2 were observed in the aromatic region (Figure S1a). The ^{1}H NMR spectra of **2** and **3** were consistent with those reported.[25] The proton signals of the dppe and PA ligands of **3T** were similar to those of **2**. In addition, the three signals from L2, one singlet and two doublets, appeared at ~8 ppm. The peak area ratios of the signals from L2 to those from dppe and PA were consistent with the expected structure, indicating that the expected triangular trimer was obtained (Figure S1b).

The structures of the $IrAu_{12}$ assemblies were observed by the HAADF-STEM. We first prepared the TEM samples by the conventional method of dropping the DCM solution of the sample onto the TEM grid with carbon support, followed by spontaneous drying. Figure S2 shows a typical TEM image of **2** prepared in this way. Highly dense white dots, corresponding to the $IrAu_{12}$, were observed in certain areas, as is often the case for various nanoparticle systems,[33] preventing us from concluding that **2** is selectively formed. These clustered images suggest that the interaction between **2** is stronger than that between **2** and the carbon support. Therefore, we added PS (average M_w~50 kDa) to the sample solution in hopes of suppressing the clustering of **2** by trapping them individually in the nano-sized voids formed in the PS films.[34] Figure 2a shows the representative HAADF-STEM image of **2** obtained by using the DCM solution of PS (PS/cluster = 5000/1 (w/w)) as the solvent. The $IrAu_{12}$ units of **2** are well dispersed with reasonable density. The TEM samples of **1** and **3T** were also prepared using the DCM solution of PS, while those of **3** were prepared using the DCM/MeCN (50/1 (v/v)) mixed solution of PS due to the low solubility of **3** in DCM. As circled in Figure 2a, a visual guide, the TEM observation supports the efficient formation of dimers in **2**, linear trimers in **3**, and triangular trimers in **3T**.

To further solidify the evidence for programmed assembly of NCs based on the obtained TEM images, the distributions of the first and second nearest neighbor distances (NND_1 and NND_2, respectively) of the $IrAu_{12}$ units were statistically analyzed. As shown in Figure 2b, the NND_1 and NND_2 for a given particle p_0 are defined as the distances to the first and second nearest neighbor particles (p_1 and p_2, respectively). In the following, the analysis method is explained using **1** as an example. First, we identified the position of the core centers in the TEM image (Figure S3). Then, the NND_1 and NND_2 values were determined for all the particles seen in Figure S3 and are shown in the histogram (Figures 2c, 2d). Finally, the histograms of NND_1 and NND_2 were compared with the probability density

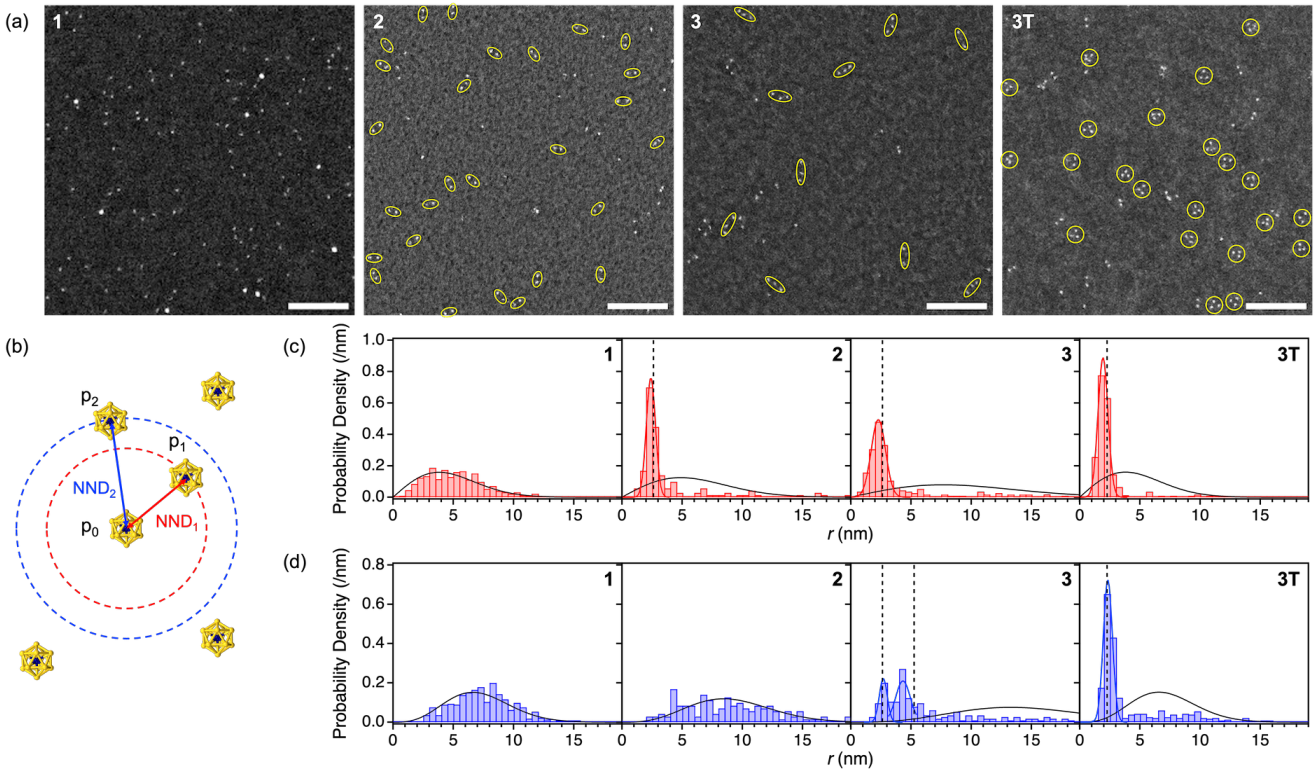

Figure 2. (a) Representative STEM images of **1**, **2**, **3**, and **3T**. Scale bars are 20 nm. (b) Schematic illustration of the NND concept. (c) NND_1 and (d) NND_2 distributions of each sample. The black curves in (c) and (d) are the calculated NND_1 and NND_2 distributions in the randomly dispersed model, respectively. The red curves in (c) and the blue curves in (d) represent the best-fit Gaussian curves. The fitting ranges were 0–4 nm, except for **3**, which was 0–5.5 nm. The vertical dotted lines in (c) and (d) indicate the distance between the core in the oligomers expected by DFT calculation.

functions $f_1(r)$ and $f_2(r)$ theoretically predicted for randomly dispersed particles:[35]

$$f_1(r) = 2\pi\rho r e^{-\pi\rho r^2} \quad (1)$$

$$f_2(r) = 2\pi^2\rho^2 r^3 e^{-\pi\rho r^2} \quad (2)$$

where r and ρ are the interparticle distance and the particle density, respectively. The ρ value for **1** (Figure S3) was 0.0109 nm^{-2} (449 particles in a 206 nm square). Both the experimental NND_1 and NND_2 distributions agreed with the theoretically calculated $f_1(r)$ and $f_2(r)$ (Figures 2c, 2d). Therefore, we concluded that the individual particles of **1** are randomly distributed within the PS network formed on the TEM grid.

Encouraged by this successful application of the statistical analysis, we extended the analysis to the images of the $IrAu_{12}$ assemblies. Figure 2c shows the experimental NND_1 histogram of **2**, which has a peak in the 2.0–2.5 nm bin, while the NND_2 histogram in Figure 2d has a broad distribution. The experimental NND_1 histogram for **2** does not agree with the $f_1(r)$ function which is predicted for randomly dispersed particles by using ρ = 0.0067 nm^{-2} (143 particles in a 146 nm square, Figure S4). This discrepancy indicates that each particle is located at an average distance of 2.4±0.4 nm. The NND_1 and NND_2 distributions of **3** and **3T** were obtained from the images in Figures S5 and S6, respectively. The NND_1 and NND_2 histograms of **3** and **3T** (Figures 2c, 2d) differ significantly reflecting the different arrangement of the three $IrAu_{12}$ units. The NND_1 histogram of **3** has a single peak at an average distance of 2.3±0.6 nm (Figure 2c), while the NND_2 histogram has two peaks at average distances of 2.7±0.3 and 4.3±0.6 nm (Figure 2d). In contrast, the NND_1 and NND_2 histograms for **3T** have single peaks at an average distances of 1.9±0.4 nm (Figure 2c) and 2.3±0.4 nm (Figure 2d), respectively.

To rationalize the results shown in Figures 2c and 2d, the DFT calculation was performed using the model structures **2-m**, **3-m**, and **3T-m**, by simplifying the dppe ligand with the dmpe ligand ($(Me)_2PC_2H_4P(Me)_2$). The optimized structures of **2-m**, **3-m**, and **3T-m** obtained at the level of B3LYP/LanL2DZ (Au, Ir) and 6-31G(d) (others) levels are shown in Figure S7. As expected, the $IrAu_{12}$ units are assembled by L1 and L2 ligands through the Au–CN coordination bonds. Close inspection revealed that the phenyl rings in L1 and L2 are not coplanar due to steric repulsion between the hydrogens of the phenyl rings, resulting in the disruption of the π-electron conjugation between them. According to the optimized structure of **2-m**, the center-to-center distance between the two $IrAu_{12}$ units was 2.6 nm (Figure S7a). Thus, the TEM results and the average NND_1 value of 2.4±0.4 nm for **2** quantitatively support that the L1 ligand binds two $IrAu_{12}$ units. The slightly shorter experimental NND_1 distance than the calculated NND_1 value is probably due to the tilted configuration of the L1 ligand in **2** with respect to the electron beam. The optimized structure of **3-m** predicts that three $IrAu_{12}$ units are linearly aligned at equivalent distances of 2.6 nm (Figure S7b). Thus, the average NND_1 and NND_2 values of 2.3±0.6 and 2.7±0.3 nm, respectively, are assigned to the first- and second-nearest-neighbor distances from the central core of **3**. Meanwhile, the average NND_2 value of 4.3±0.6 nm is assigned to the distance between the two terminal cores of **3**. The optimized structure of **3T-m** predicts that three $IrAu_{12}$ units are triangularly aligned at a distance of 2.3 nm (Figure S7c). This structure explains the average NND_1 and NND_2 values of 1.9±0.4 and 2.3±0.4 nm for **3T**. In conclusion, the NND analysis and DFT calculations support the successful assembly of the $IrAu_{12}$ units in a programmed manner as shown in Scheme 1. We further

investigated the chemical identity of individual particles in the assembly using energy dispersive X-ray spectroscopy (EDS). As shown in a STEM-EDS elemental mapping of **2** (Figure S8), both Ir and Au signals were detected at the position of individual $IrAu_{12}$ particles. Quantitative analysis estimated the atomic ratio of Au/Ir to be 12.2±3.6, supporting the composition of the $IrAu_{12}$ units.

We then attempted to prepare and observe the linear oligomers longer than **3**. The oligomers of the $IrAu_{12}$ units were prepared by mixing $^{*}\mathbf{1}^{*}$ with 0.9 eq. of L1. Figure 3a shows the typical ESI mass spectrum of the as-prepared linear oligomers dissolved in MeCN. Instead of the expected oligomers with exposed and/or L1-terminated ends, such as $(^{*}\mathbf{1}^{*}\text{–L1})_{n-1}\text{–}^{*}\mathbf{1}^{*}$, $\text{L1–}(^{*}\mathbf{1}^{*}\text{–L1})_{n-1}\text{–}^{*}\mathbf{1}^{*}$, and $\text{L1–}(^{*}\mathbf{1}^{*}\text{–L1})_{n}$, the most dominant species observed were $\text{Cl–}(^{*}\mathbf{1}^{*}\text{–L1})_{n-1}\text{–}^{*}\mathbf{1}^{*}\text{–Cl}$ and $\text{L1–}(^{*}\mathbf{1}^{*}\text{–L1})_{n-1}\text{–}^{*}\mathbf{1}^{*}\text{–Cl}$ with n = 2–10 (Figure S9). This indicates that the oligomers' exposed ends are highly reactive, even toward Cl-containing impurities present in the mass spectrometer. The longest oligomer detected by ESI-MS was the decamer $\text{Cl–}(^{*}\mathbf{1}^{*}\text{–L1})_{9}\text{–}^{*}\mathbf{1}^{*}\text{–Cl}$ adducted with nine BF_4^- counteranions. The representative HAADF-STEM image of the oligomers is shown in Figure 3b: the TEM sample was prepared by using the DCM/MeCN (50/1) mixed solution of PS as a solvent. As expected, linear oligomers ranging from the dimer to the hexamer are observed. For example, a closer look at the hexamer (Figure 3c) shows that the interparticle distances were in the range of 2.3–2.7 nm, which is close to that of the theoretically optimized structures of **2-m** and **3-m** (Figures S7a, S7b). The bent structure indicates that the linear oligomers exhibit a certain degree of structural flexibility.

The electronic structures of the assemblies were studied theoretically using the DFT-optimized structures **2-m** (Figure S7a) and **3-m** (Figure S7b). The energy levels and shapes of the Kohn-Sham orbitals for **2-m** and **3-m** obtained in the CAM-B3LYP/LanL2DZ (Au, Ir) and 6-31G(d) (others) levels are shown in Figures 4a and 4b, respectively. Starting with **2-m**, the occupied orbitals are localized on one of the $[IrAu_{12}(dmpe)_5(PA)_1]^{2+}$ (**1-m***) units and doubly degenerate (Figure 4a), so in the following we focus only on the nature of the highest occupied molecular orbital (HOMO), HOMO-2 and HOMO-4. The HOMO and HOMO-2 are constructed by

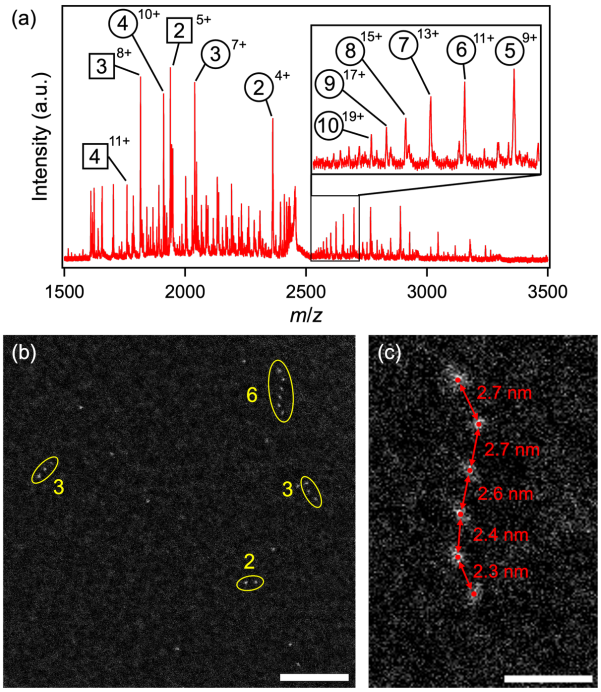

Figure 3. (a) ESI mass spectrum of linear oligomers of $^{*}\mathbf{1}^{*}$. The numbers in the circles and squares indicate the n values for $\text{Cl–}(^{*}\mathbf{1}^{*}\text{–L1})_{n-1}\text{–}^{*}\mathbf{1}^{*}\text{–Cl}$ and $\text{L1–}(^{*}\mathbf{1}^{*}\text{–L1})_{n-1}\text{–}^{*}\mathbf{1}^{*}\text{–Cl}$, respectively. Detailed assignment is given in Figure S9. (b) Typical HAADF-STEM image of linear oligomers of $^{*}\mathbf{1}^{*}$. The scale bar is 20 nm. (c) Enlarged HAADF-STEM image of the hexamer. The scale bar is 5 nm.

bonding and anti-bonding interactions between the π orbital of the terminal PA ligand and the 1P superatomic orbital of the **1-m*** unit, respectively (Figure 4a).[25] HOMO-4 is constructed by the bonding interaction between the π orbitals of L1 and the 1D superatomic orbitals of the **1-m*** units, which can be better understood by representing them with the isovalue of 0.001 (Figure S12). In contrast, the contribution of the π orbital of L1 becomes evident in the unoccupied orbitals (Figure 4a): the lowest unoccupied molecular orbital (LUMO) is composed of

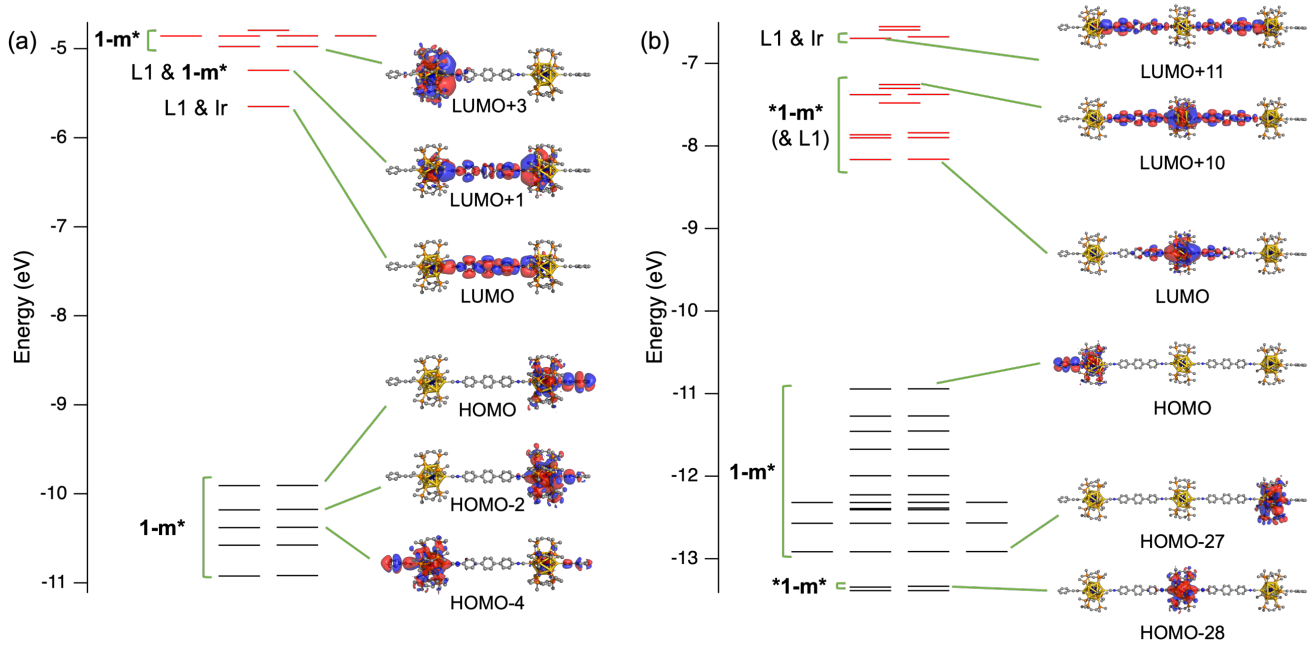

Figure 4. Energy diagram and representative KS orbitals (isovalue = 0.008) of (a) **2-m** and (b) **3-m**.

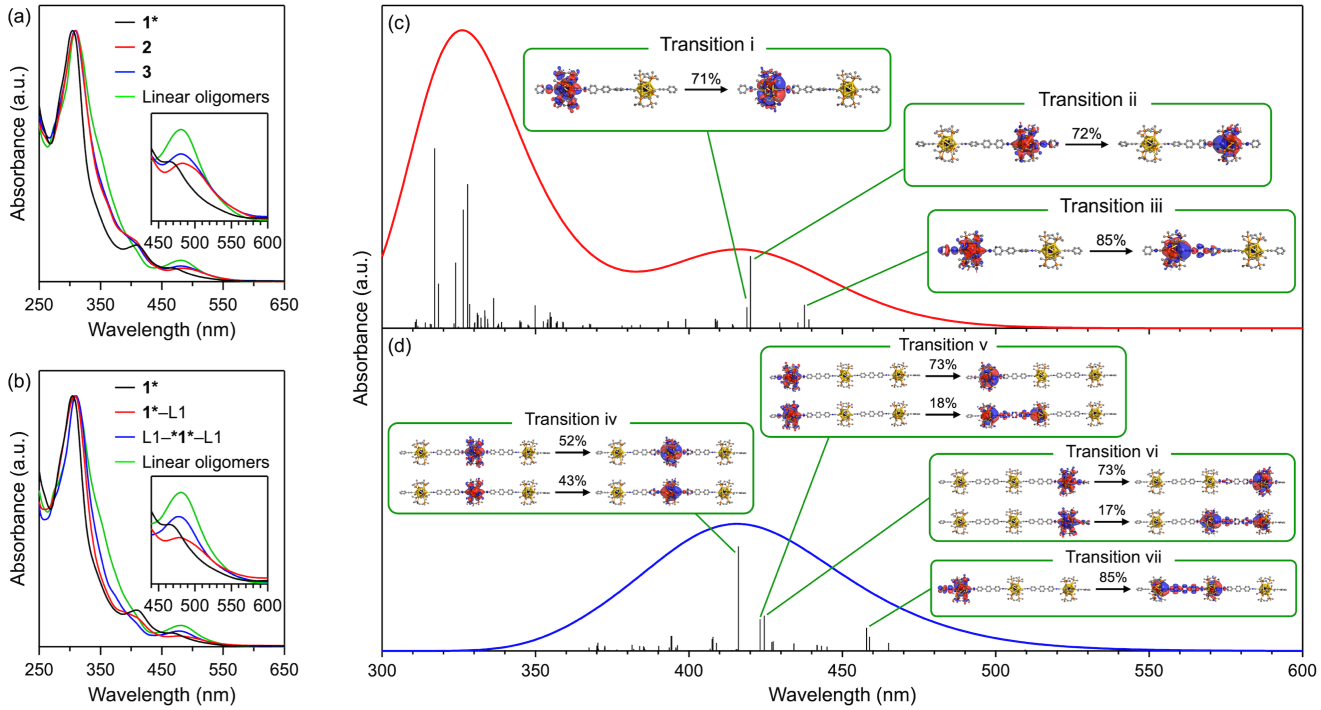

Figure 5. UV-vis absorption spectra of (a) **1***, **2**, **3**, and linear oligomers of *__1__* and (b) **1***, **1***–L1, L1–*__1__*–L1, and linear oligomers of *__1__* in MeCN. Each spectrum was normalized to the most intense peak. Simulated UV-vis absorption spectra of (c) **2-m** and (d) **3-m**. The natural transition orbitals (isovalue = 0.008) of the representative transitions were displayed as insets.

the π orbital of L1 and the 5d orbitals of the Ir atoms, while the LUMO+1 is composed of the π orbital of the L1 ligand and the 1D orbital of the **1-m*** unit. Next, the HOMO to HOMO-27 of **3-m** are mainly localized to one of the terminal **1-m*** units, while HOMO-28 and HOMO-29 are mainly localized to the central $[IrAu_{12}(dmpe)_5]^{3+}$ (*__1__-__m__*) unit (Figure 4b). In contrast, the LUMO to LUMO+10 are mainly contributed by the central *__1__-__m__* unit, while the LUMO+11 and LUMO+12 consist of π (L1) and 5d (Ir) orbitals. In summary, the introduction of the *__1__-__m__* unit into **2-m** significantly changes the energy ordering of the unoccupied MOs.

The evolution of the optical properties of the linear assemblies as a function of the number of $IrAu_{12}$ units was investigated by comparing the UV-vis absorption spectra of **1***, **2**, **3**, and linear oligomers of *__1__* (Figure 5a). The molar absorption coefficients (ε_{max}) of **1***, **2**, and **3** at 304, 310, and 309 nm were 1.5×10^5, 2.9×10^5, and 4.6×10^5 $M^{-1}cm^{-1}$, respectively (Figure S10), indicating that the ε_{max} value of the linear assembly increases linearly with the number of the $IrAu_{12}$ units. The spectral profiles were then compared after normalization to the most intense peak. A new peak appeared at ~480 nm for **2** and became more pronounced with the number of the $IrAu_{12}$ units (Figure 5a). To determine whether this new peak was related to the difference between the PA and L1 ligands on the $IrAu_{12}$ units, the compounds L1–*__1__*–L1 and **1***–L1 were synthesized as references (Figure S11). The absorption spectra of L1–*__1__*–L1 and **1***–L1 are compared with that of **1*** in Figure 5b after normalization at 310 nm. The absorbance at 480 nm increased in the order of **1*** < **1***–L1 < L1–*__1__*–L1, suggesting that the ligation of L1 is responsible for the peak at 480 nm. However, the absorbance at 480 nm of the oligomers without PA ligands is significantly greater than that of L1–*__1__*–L1. This indicates that the number of the assembled $IrAu_{12}$ units also contributes to the appearance of the 480 nm peak.

Finally, the absorption spectra of **2-m** and **3-m** were theoretically simulated by TD-CAM-B3LYP/LanL2DZ (Au, Ir) and 6-31G(d) (others) to help assign the experimental spectra. The results are summarized in Figure 5c and d. First, the simulated spectrum of **2-m** (Figure 5c) qualitatively reproduces the spectral features of **2** (Figure 5a, red) although the lowest energy peak is slightly blue-shifted. The main contributors to the lowest energy band at ~415 nm are three transitions i–iii, whose assignments are given in Table S3. In the following, the optical transition is discussed based on the results of the natural transition orbital (NTO) analysis[36] rather than using the canonical orbitals to capture the essence of the transition. As shown in Figure 5c, the transitions i and ii are mainly assigned to local excitation within the **1-m*** unit, while the lowest energy transition iii can be considered as an electron transfer from **1-m*** to L1. These results suggest that transition iii is responsible for the appearance of the new absorption band at 480 nm for **2** (Figure 5a, red). Next, the simulated spectrum of **3-m** also shows the lowest energy band at ~415 nm (Figure 5d), like **2-m** (Figure 5c). This negligible shift in the peak position reproduces the experimental results (Figure 5a, blue). The main contributors to the lowest energy band are four transitions iv–vii, whose assignments are summarized in Table S4. The most intense transition iv is a localized excitation within the central *__1__-__m__* unit, while transitions v and vi correspond to the localized excitation within the terminal **1-m*** unit with a slight contribution from the electron transfer from the terminal **1-m*** to the central *__1__-__m__* (Figure 5d). The lowest energy transition vii is considered mainly as an electron transfer from the terminal **1-m*** unit to the central *__1__-__m__* unit (Table S4). In summary, the absorption peak at 480 nm for **3** contains the contribution of electron transfer from the terminal **1-m*** units to the central *__1__-__m__* unit. Further enhancement of the absorbance at 480 nm for the longer linear assemblies of *__1__* (Figure 5a, green) suggests a greater involvement of the inter-cluster electron transfer.

In summary, we have achieved the programmed assembly of the icosahedral $Ir@Au_{12}$ nanoclusters into a dimer, a linear

trimer, linear oligomers, or a triangular trimer via the reaction between the $IrAu_{12}$ units with predefined binding sites and multidentate isocyanide linkers. A newly developed protocol for the EM sample preparation allowed us to confirm the formation of the programmed assembled structures as the major species. In addition, statistical analysis of the nearest neighbor distances between the $IrAu_{12}$ units provided quantitative structure models that were consistent with the DFT-optimized structures. Optical absorption spectroscopy of the linear assemblies revealed a new peak at 480 nm in the dimer, which becomes more pronounced in the trimer. TD-DFT calculations revealed that the peak growth is due to the electron transfer from the $IrAu_{12}$ unit to the linker ligand in the dimer and to another $IrAu_{12}$ unit in the trimer. Bottom-up, programmed assembly of pre-defined Au nanoclusters will provide us with an opportunity to elucidate how novel collective properties of Au nanoclusters arise through assembly.

ASSOCIATED CONTENT

Supporting Information: Synthetic details and ESI-MS spectrum. This material is available free of charge via the Internet at http://pubs.acs.org.

AUTHOR INFORMATION

Corresponding Authors

harano.koji@nims.go.jp
tsukuda@chem.s.u-tokyo.ac.jp

ACKNOWLEDGMENT

This research was financially supported by JST, CREST (Grant No. JPMJCR20B2) and by JSPS KAKENHI Grant Numbers (JP23H00284, JP23H01917, JP23H04874, and JP25KJ0897) and the World-leading Innovative Graduate Study Program for Materials Research, Information, and Technology (MERIT-WINGS) from the University of Tokyo. Part of the computations were performed at the Research Center for Computational Science, Okazaki, Japan (Project: 24-IMS-C158). Part of the electron microscopy experiments was supported by the Electron Microscopy Unit, National Institute for Materials Science (NIMS).

REFERENCES

(1) Jin, R.; Zeng, C.; Zhou, M.; Chen, Y. Atomically Precise Colloidal Metal Nanoclusters and Nanoparticles: Fundamentals and Opportunities. *Chem. Rev.* **2016**, *116*, 10346–10413.

(2) Chakraborty, I.; Pradeep, T. Atomically Precise Clusters of Noble Metals: Emerging Link between Atoms and Nanoparticles. *Chem. Rev.* **2017**, *117*, 8208–8271.

(3) Kang, X.; Li, Y.; Zhu, M.; Jin, R. Atomically Precise Alloy Nanoclusters: Syntheses, Structures, and Properties. *Chem. Soc. Rev.* **2020**, *49*, 6443–6514.

(4) Omoda, T.; Takano, S.; Tsukuda, T. Toward Controlling the Electronic Structures of Chemically Modified Superatoms of Gold and Silver. *Small* **2021**, *17*, 2001439.

(5) Chakraborty, P.; Nag, A.; Chakraborty, A.; Pradeep, T. Approaching Materials with Atomic Precision Using Supramolecular Assemblies. *Acc. Chem. Res.* **2019**, *52*, 2–11.

(6) Kang, X.; Zhu, M. Intra-Cluster Growth Meets Inter-Cluster Assembly: The molecular and Supramolecular Chemistry of Atomically Precise Nanoclusters. *Coord. Chem. Rev.* **2019**, *394*, 1–38.

(7) Wu, Z.; Yao, Q.; Zang, S.; Xie, J. Directed Self-Assembly of Ultrasmall Metal Nanoclusters. *ACS Mater. Lett.* **2019**, *1*, 237–248.

(8) Ebina, A.; Hossain, S.; Horihata, H.; Ozaki, S.; Kato, S.; Kawawaki, T.; Negishi, Y. One-, Two-, and Three-Dimensional Self-Assembly of Atomically Metal Nanoclusters. *Nanomaterials* **2020**, *10*, 1105.

(9) Yao, Q.; Wu, Z.; Liu, Z.; Lin, Y.; Yuan, X.; Xie, J. Molecular Reactivity of Thiolate-Protected Noble Metal Nanoclusters: Synthesis, Self-Assembly, and Applications. *Chem. Sci.* **2021**, *12* , 99–127.

(10) Bonacchi, S.; Antonello, S.; Dainese, T.; Maran, F. Atomically Precise Metal Nanoclusters: Novel Building Blocks for Hierarchical Structures. *Chem. – Euro. J.* **2021**, *27*, 30–38.

(11) Saito, Y.; Murata, C.; Sugiuchi, M.; Shichibu, Y.; Konishi, K. Ligand-Coordinated Metal Clusters in Condensed States: Self-Assemblies, Crystals, and Covalent Networks. *Coord. Chem. Rev.* **2022**, *470*, 214713.

(12) Banach, E.; Bürgi, T. Metal Nanoclusters as Versatile Building Blocks for Hierarchical Structures. *Helv. Chim. Acta.* **2022**, *105*, e202100186.

(13) Maity, S.; Kolay, S.; Chakraborty, S.; Devi, A.; Rashi; Patra, A. A Comprehensive Review of Atomically Precise Metal Nanoclusters with Emergent Photophysical Properties towards Diverse Applications. *Chem. Soc. Rev.* **2025**, *54*, 1785–1844.

(14) Yao, Q.; Luo, Z.; Yuan, X.; Yu, Y.; Zhang, C.; Xie, J.; Lee, J. Y. Assembly of Nanoions via Electrostatic Interactions: Ion-Like Behavior of Charged Noble Metal Nanoclusters. *Sci. Rep.* **2014**, *4*, 3848.

(15) Zeng, C.; Chen, Y.; Kirschbaum, K.; Lambright, K. J.; Jin, R. Emergence of Hierarchical Structural Complexities in Nanoparticles and Their Assembly. *Science,* **2016**, *354*, 1580–1584.

(16) Li, Y.; Zhou, M.; Song, Y.; Higaki, T.; Wang, H.; Jin, R. Double-Helical Assembly of Heterodimeric Nanoclusters into Supercrystals. *Nature* **2021**, *594*, 380–384.

(17) Kim, S.; Kim, H.; Lee, C.; Park Ina and Kim, Y.; Moon, D.; Shim, J. H.; Ryu, S.; Park, S. S. Au_{25} Cluster-Based Atomically Precise Coordination Frameworks and Emission Engineering through Lattice Symmetry. *ACS Nano* **2024**, *18*, 29036–29044.

(18) Lahtinen, T.; Hulkko, E.; Sokołowska, K.; Tero, T.-R.; Saarnio, V.; Lindgren, J.; Pettersson, M.; Häkkinen, H.; Lehtovaara, L. Covalently Linked Multimers of Gold Nanoclusters Au_{102}(p-MBA)$_{44}$ and $Au_{\sim 250}$(p-MBA)$_n$. *Nanoscale* **2016**, *8*, 18665–18674.

(19) Sokolowska, K.; Hulkko, E.; Lehtovaara, L.; Lahtinen, T. Dithiol-Induced Oligomerization of Thiol-Protected Gold Nanoclusters. *J. Phys. Chem. C* **2018**, *122*, 12524–12533.

(20) Sels, A.; Salassa, G.; Cousin, F.; Lee, L.-T.; Bürgi, T. Covalently Bonded Multimers of Au_{25}(SBut)$_{18}$ as a Conjugated System. *Nanoscale* **2018**, *10*, 12754–12762.

(21) Ho-Wu, R.; Sun, K.; Goodson, T. I. I. I. Synthesis and Enhanced Linear and Nonlinear Optical Properties of Chromophore–Au Metal Cluster Oligomers. *J. Phys. Chem. C* **2018**, *122*, 2315–2329.

(22) Swierczewski, M.; Cousin, F.; Banach, E.; Rosspeintner, A.; Lawson Daku, L. M.; Ziarati, A.; Kazan, R.; Jeschke, G.; Azoulay, R.; Lee, L.-T.; Bürgi, T. Exceptionally Stable Dimers and Trimers of Au_{25} Clusters Linked with a Bidentate Dithiol: Synthesis, Structure and Chirality Study. *Angew. Chem., Int. Ed.* **2023**, *62*, e202215746.

(23) Kito, N.; Takano, S.; Masuda, S.; Harano, K.; Tsukuda, T. Au_{13} Superatom Bearing Two Terpyridines at Coaxial Positions: Photoluminescence Quenching via Complexation with 3d Metal Ions. *Bull. Chem. Soc. Jpn.* **2023**, *96*, 1045–1051.

(24) Kosaka, T.; Niihori, Y.; Kawawaki, T.; Negishi, Y. Synthesis of Au_{13}-Based Building Block Clusters for

Programmed Dimer Formation and Au_{13} Cluster Dimer Photoexcitation Properties. *Nanoscale* **2025**, *17*, 12695–12703.
(25) Fukumoto, Y.; Omoda, T.; Hirai, H.; Takano, S.; Harano, K.; Tsukuda, T. Diphosphine-Protected $IrAu_{12}$ Superatom with Open Site(s): Synthesis and Programmed Stepwise Assembly. *Angew. Chem., Int. Ed.* **2024**, *63*, e202402025.
(26) Negishi, Y.; Tsunoyama, H.; Yanagimoto, Y.; Tsukuda, T. Subnanometer-Sized Gold Clusters with Dual Molecular Receptors: Synthesis and Assembly in One-Dimensional Arrangements. *Chem. Lett.* **2005**, *34*, 1638–1639.
(27) Yao, Q.; Luo, Z.; Yuan, X.; Yu, Y.; Zhang, C.; Xie, J.; Lee, J. Y. Assembly of Nanoions via Electrostatic Interactions: Ion-Like Behavior of Charged Noble Metal Nanoclusters. *Sci. Rep.* **2014**, *4*, 3848.
(28) Compel, W. S.; Wong, O. A.; Chen, X.; Yi, C.; Geiss, R.; Häkkinen, H.; Knappenberger, K. L. Jr.; Ackerson, C. J. Dynamic Diglyme-Mediated Self-Assembly of Gold Nanoclusters. *ACS Nano* **2015**, *9*, 11690–11698.
(29) Wen, Z.-R.; Guan, Z.-J.; Zhang, Y.; Lin, Y.-M.; Wang, Q.-M. $[Au_7Ag_9(Dppf)_3(CF_3CO_2)_7BF_4]_n$: A Linear Nanocluster Polymer from Molecular Au_7Ag_8 Clusters Covalently Linked by Silver Atoms. *Chem. Commun.* **2019**, *55*, 12992–12995.
(30) Wu, Z.; Du, Y.; Liu, J.; Yao, Q.; Chen, T.; Cao, Y.; Zhang, H.; Xie, J. Aurophilic Interactions in the Self-Assembly of Gold Nanoclusters into Nanoribbons with Enhanced Luminescence. *Angew. Chem., Int. Ed.* **2019**, *58*, 8139–8144.
(31) Yao, Q.; Liu, L.; Malola, S.; Ge, M.; Xu, H.; Wu, Z.; Chen, T.; Cao, Y.; Matus, M. F.; Pihlajamäki, A.; Han, Y.; Häkkinen, H.; Xie, J. Supercrystal Engineering of Atomically Precise Gold Nanoparticles Promoted by Surface Dynamics. *Nat. Chem.* **2023**, *15*, 230–239.
(32) Saito, Y.; Sun, D.; Kanai, H.; Ishida, Y.; Mitomo, H.; Ijiro, K.; Konishi, K. Charge-Dependent Hierarchical Self-Assembling of Fluorinated Gold Nanoclusters. *Chem. Commun.* **2025**, *61*, 1383–1386.
(33) Michen, B.; Geers, C.; Vanhecke, D.; Endes, C.; Rothen-Rutishauser, B.; Balog, S.; Petri-Fink, A. Avoiding Drying-Artifacts in Transmission Electron Microscopy: Characterizing the Size and Colloidal State of Nanoparticles. *Sci. Rep.* **2015**, *5*, 9793.
(34) Pethrick, R. A. Positron Annihilation–A Probe for Nanoscale Voids and Free Volume? *Prog. Polym. Sci.* **1997**, *22*, 1–47.
(35) Thompson, H. R. Distribution of Distance to Nth Neighbour in a Population of Randomly Distributed Individuals. *Ecology* **1956**, *37*, 391–394.
(36) Martin, R. L. Natural Transition Orbitals. *J. Chem. Phys.* **2003**, *118*, 4775–4777.